Volume 15, Issue 3, 152423 (1-12)

International Journal of Nano Dimension (IJND)

https://dx.doi.org/10.57647/j.ijnd.2024.1503.23

Comparative study on Pb^{2+} adsorption using spinel nanostructures-embedded graphene oxide

Mahnaz Parastar Gharehlar, Shabnam Sheshmani*, Farrokh Roya Nikmaram, Zohreh Doroudi

Department of Chemistry, College of Basic Sciences, Yadegar-e-Imam Khomeini (RAH) Shahre Rey Branch, Islamic Azad University, Tehran, Iran.

*Corresponding author: shabnam_sheshmani@yahoo.com

Original Research

Received:
7 March 2024
Revised:
10 May 2024
Accepted:
14 May 2024
Published online:
15 June 2024

Abstract:

This study investigates the adsorption performance of spinel nanostructures-embedded graphene oxide (GO) for removing toxic Pb^{2+} ions from water. The graphene oxide nanocomposites containing Fe_3O_4, $CoFe_2O_4$, and $NiFe_2O_4$ nanoparticles were synthesized and characterized. The $NiFe_2O_4$/GO nanocomposite exhibited the highest Pb^{2+} adsorption capacity, reaching 96.1% removal at 75 minutes contact time with initial Pb^{2+} concentration of 10 ppm. The $CoFe_2O_4$/GO nanocomposite achieved 90.3% Pb^{2+} removal under similar conditions, while Fe_3O_4/GO showed 88.8%. Kinetic studies revealed the adsorption followed a pseudo-second-order model with R^2 values of 0.99-1.00. The adsorption mechanism involves surface adsorption on GO sheets and spinel nanoparticles. The nanocomposites demonstrated good recyclability, maintaining over 65% removal efficiency after three consecutive cycles. This study provides insights into designing effective adsorbents for mitigating potentially toxic elements pollution in water, addressing environmental and public health challenges.

Keywords: $CoFe_2O_4$/GO; Fe_3O_4/GO; $NiFe_2O_4$/GO; Graphene oxide; Pb^{2+} Removal; Spinel

1. Introduction

Potentially toxic elements pollution is a significant environmental and health concern. Industrial activities, mining, improper waste disposal, and consumer products contribute to the accumulation of toxic elements like lead in the environment. This contamination disrupts ecosystems, contaminates air, soil, and water, and poses health risks, including neurological disorders and cancer [1, 2]. Lead is a highly toxic and persistent threat with significant health implications. Exposure occurs through contaminated water, food, and inhalation of lead particles. Lead is highly toxic, especially for children's developing brains, causing learning disabilities, decreased IQ, ADHD, and impaired cognition. Prenatal exposure can lead to low birth weight, premature birth, and developmental delays. Lead interferes with red blood cell production, causing anemia, fatigue, and reduced oxygen transport. Prolonged exposure damages kidneys, increasing risks of chronic kidney disease and hypertension. It elevates cardiovascular risks like heart attacks and strokes. It accumulates in bones, interfering with formation/remodeling, leading to low bone density, osteoporosis, and fracture risk. Ingestion causes gastrointestinal issues like abdominal pain, nausea, vomiting, and constipation. Mitigating lead exposure is crucial for safeguarding public health, especially vulnerable groups like children and pregnant women [3–5].

Efforts to mitigate toxic elements pollution, particularly lead contamination, have spurred research on efficient water adsorbents. Adsorption is favored for its simplicity, cost-effectiveness, and high removal efficiency. Specially designed adsorbent materials with large surface areas selectively capture and remove toxic elements ions from water sources. While natural and conventional adsorbents like clays, agricultural waste, and activated carbon have been explored, innovative nanocomposite materials show promising adsorption capabilities for toxic elements removal [4–12]. Innovative material design, surface modification, and incorporation of nanomaterials have resulted in highly porous

and reactive adsorbents with impressive toxic elements removal capabilities. Additionally, combining adsorption with techniques like membrane filtration and advanced oxidation processes show promise for comprehensive water purification. Ongoing research aims to develop efficient and cost-effective adsorbents that have the potential to revolutionize toxic elements pollution mitigation in water, safeguarding public health, and preserving water resources.

Graphene oxide-embedded spinel nanostructures are promising adsorbents for removing toxic elements from water. These composites combine the exceptional properties of graphene oxide, such as high surface area and functional groups, with the robust structure and magnetic properties of spinel nanoparticles like. The synergy between the two components enhances adsorption capabilities, selectivity, and separation efficiency. These composite adsorbents offer advantages such as high binding capacity, efficient removal, stability, reusability, and potential customization. With further optimization, these innovative adsorbents could contribute to more effective and sustainable strategies for mitigating toxic element pollution, safeguarding water resources, and protecting public health [13–16]. However, a systematic investigation comparing the adsorption performance of different spinel-GO nanocomposites for lead removal is lacking.

This work presents an experimental study evaluating the performance of spinel nanostructures-embedded graphene oxide for adsorbing Pb^{2+} ions. The study investigates the adsorption efficiency and operational parameters of these nanocomposites. Different graphene oxide-spinel nanocomposites are examined to understand the relationship between properties and Pb^{2+} affinity. Characterization techniques probe surface chemistry, morphology, and adsorbent-Pb^{2+} interactions. The study establishes optimal conditions for maximizing adsorption efficiency and provides insights for real-world water treatment applications. The findings contribute to knowledge and guide the design of adsorbents for removing toxic element contaminants from water. This work accelerates the development of sustainable solutions for mitigating toxic elements pollution, addressing public health and ecosystem preservation challenges.

2. Experiments

2.1 Materials

The materials utilized in this study were ferric chloride ($FeCl_3$, 98% purity, Merck), ferrous chloride tetrahydrate ($FeCl_2 \cdot 4H_2O$, 98% purity, Merck), cobalt chloride hexahydrate ($CoCl_2 \cdot 6H_2O$, 98% purity, Merck), nickel nitrate hexahydrate ($Ni(NO_3)_2 \cdot 6H_2O$, 98% purity, Merck), lead nitrate ($Pb(NO_3)_2$, 99.9% purity, Sigma-Aldrich), graphite flakes (99.5% purity, Sigma-Aldrich), potassium chlorate ($KClO_3$, 99.5% purity, Merck), nitric acid (HNO_3, 65% purity, Merck), sulfuric acid (H_2SO_4, 98% purity, Merck), hydrochloric acid (HCl, 37% purity, Merck), and aqueous ammonia (NH_3(aq), 25% purity, Merck).

2.2 Methods

XRD patterns were obtained using a PHILIPS PW1730 instrument with Cu Kα radiation, within a 2θ range of 10 to 80°. The patterns were analyzed and indexed using the JCPDS database files. Fourier transform infrared spectroscopy (FT-IR) measurements were conducted using Thermo AVATAR equipment across the 500-4000 cm^{-1} range. The morphology and particle size were examined using a TESCAN MIRA III electron microscope operating in SEM mode. Before imaging, samples were coated with a thin layer of gold for improved resolution. The metal concentrations were measured using flame atomic absorption spectrometry (Varian AA-1275). Ultrasonic apparatus (Elmasonic 60H) and centrifuge (Universal 320 Hettich) were used.

2.3 Stock solution of Pb(II) ions

To prepare the stock solution of Pb(II) ions, $Pb(NO_3)_2$ were dissolved in double-distilled water, respectively, to achieve a concentration of 1000 mg/L. The resulting solutions were diluted with deionized water to obtain the desired concentrations. The initial pH of the working solution was adjusted by adding either 0.1 N HCl or 0.1 N NaOH solutions as needed.

2.4 Adsorption experiments

In the first step, adsorbent (20 mg) was added to metal solutions (0.05 g/L, 10 mL) at various pH values ranging from 3 to 7. The mixtures were allowed to interact for 20 minutes, and the optimal pH value for metal adsorption was determined. Subsequently, the effects of other parameters including sorbent dosage (0.01-0.05 g), Pb^{2+} concentration (5-40 ppm), and contact time (15-75 min.) on the adsorption of metal ions were investigated. The kinetics of sorption was determined. The percentage of metal removal (R) was calculated using the following equation:

$$R = (C_0 - C_t)/C_0 \times 100$$

C_0 represents the initial metal concentration (mg/L), and C_t represents the metal concentration (mg/L) at time t. All experiments were conducted in triplicate, and the average values were reported.

2.5 Synthesis of graphene oxide, GO

The modified Staudenmaier method was employed to synthesize graphene oxide. In this process, a mixture of nitric acid (9 mL) and sulfuric acid (27 mL) was combined and cooled in an ice bath. Gradually, graphite powder (1 g) was added to the mixture. Subsequently, potassium chlorate powder (11 g) was slowly dispersed to maintain a temperature below 20 °C. The resulting mixture was stirred at room temperature for four days. Finally, the resulting black product was washed with deionized water until reaching a pH of 7. The resulting residue, identified as graphite oxide, was dried in a vacuum oven at 60 °C [17].

2.6 Synthesis of spinel nanostructures-embedded graphene oxide

To synthesize the ferrite spinel nanostructures-embedded graphene oxide, a hydrothermal method was used. Ferric chloride ($FeCl_3$) and ferrous chloride tetrahydrate ($FeCl_2{\cdot}4H_2O$) in a molar ratio 2:1 were dissolved in 15

mL of distilled water. Aqueous ammonia (NH_3(aq)) was added gradually until the pH reached 12. Then, 0.1 g of graphene oxide was added to the solution and stirred for 30 minutes. The mixture was transferred to a Teflon autoclave and subjected to hydrothermal treatment at 180 °C for 13 hours. After cooling to room temperature, the precipitates were separated by filtration and washed with water and ethanol until the pH of the filtrate was 7. The filtered precipitates were dried in a vacuum oven at 60 °C for 12 hours to obtain the final composite.

For the synthesis of cobalt ferrite ($CoFe_2O_4$) and nickel ferrite ($NiFe_2O_4$) spinel-embedded graphene oxide (GO) composites, a similar procedure was followed. In the cobalt ferrite synthesis, iron (III) chloride hexahydrate (2 mmol) and cobalt (II) chloride hexahydrate (1 mmol) were mixed, and the pH was adjusted by gradually adding ammonium hydroxide solution (25%) until reaching pH 12. Graphene oxide (0.1 g) was added and stirred for 30 minutes. The mixture was then transferred to a Teflon autoclave and heated at 180 °C for 13 hours. After cooling to room temperature, the precipitates were separated, washed with water and ethanol, and dried in a vacuum oven at 60°C. Similarly, for the nickel ferrite embedded graphene oxide synthesis, iron (III) chloride hexahydrate (2 mmol) and nickel(II) nitrate hexahydrate (1 mmol) were mixed. Graphene oxide (0.1 g) was added, and the mixture was stirred for 30 minutes. The subsequent steps, including pH adjustment, transfer to a Teflon autoclave, heating, cooling, separation, washing, and drying, were performed using the same protocol as the $CoFe_2O_4$/GO synthesis [18]. The synthesized $CoFe_2O_4$/GO, $NiFe_2O_4$/GO, and previously prepared Fe_3O_4/GO composites underwent thorough analysis for characterization purposes. These analyses provided valuable insights into the structural properties of the composites, aiding in their further application and understanding.

3. Results and discussion

X-ray diffraction (XRD) analysis was performed to investigate the structural properties of Fe_3O_4/GO, $CoFe_2O_4$/GO, and $NiFe_2O_4$/GO nanocomposites. In the Fe_3O_4/GO composite, distinct diffraction peaks corresponding to Fe_3O_4 nanoparticles were observed at 30.2°, 35.6°, 43.1°, 53.4°, 57.2°, and 62.8°, corresponding to the crystal planes (220), (311), (400), (422), (511), and (440). These peaks served as conclusive evidence for the presence of Fe_3O_4 nanoparticles in the composite. Additionally, characteristic peaks associated with the graphene oxide phase were observed at 10.5° (002), confirming the incorporation of graphene oxide sheets within the nanocomposite structure (Fig.1) [17].

The XRD patterns of the $CoFe_2O_4$/GO and $NiFe_2O_4$/GO composites provided valuable insights into their structural properties. In the $CoFe_2O_4$/GO composite, well-defined diffraction peaks appeared at 30.7°, 35.7°, 42.6°, 57.1°, and 62.8°, corresponding to specific crystallographic planes (220), (311), (400), (511), and (440) of $CoFe_2O_4$, strongly indicating the presence of $CoFe_2O_4$ nanoparticles in the composite structure [18]. For the $NiFe_2O_4$/GO composite, prominent diffraction peaks were identified at 22°, 30.2°, 35.6°, 43.4°, 57.4°, and 63.1°, corresponding to specific planes (111), (220), (311), (400), (511), and (440) of $NiFe_2O_4$, confirming the presence of $NiFe_2O_4$ nanoparticles [18]. Clear peaks associated with the graphene oxide phase were observed at 10° for both composites, indicating the successful integration of graphene oxide within the composite structures (Figs. 2, and 3).

Overall, the XRD patterns provided compelling evidence of the respective nanoparticles and graphene oxide, affirming the successful synthesis of these nanocomposites. These findings contribute to a better understanding of their structural characteristics and pave the way for their potential applications in various fields.

The FT-IR analysis of Fe_3O_4/GO, $CoFe_2O_4$/GO, and $NiFe_2O_4$/GO nanocomposites revealed several characteristic peaks. The broad absorption band at around 3300 cm^{-1} corresponds to the stretching vibration of O-H groups.

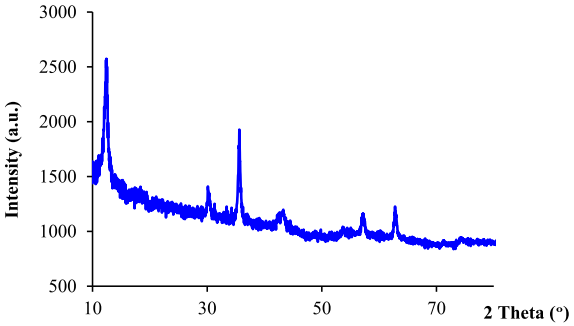

Figure 1. XRD pattern of Fe_3O_4/GO.

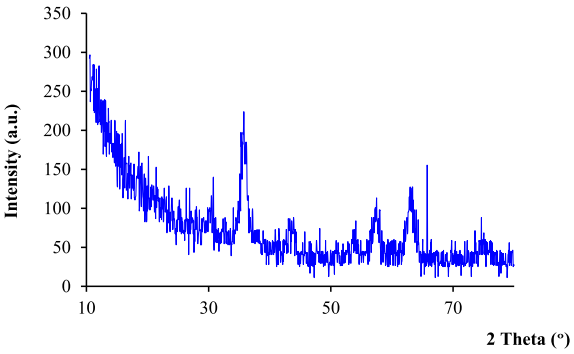

Figure 2. XRD pattern of $CoFe_2O_4$/GO.

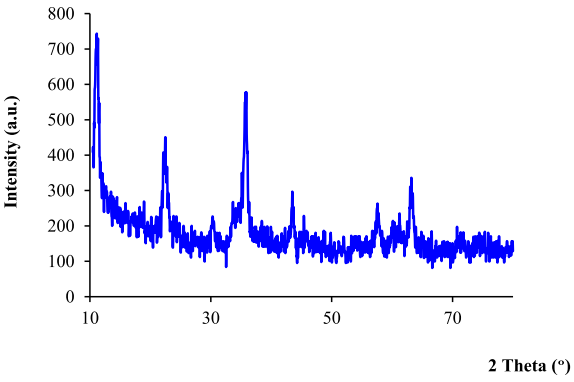

Figure 3. XRD pattern of $NiFe_2O_4$/GO.

The absorption band around 3000 cm^{-1} is primarily due to the stretching vibrations of the C-H bonds in the hydroxyl and carboxyl groups of graphene oxide. The peak observed at about 1700 and 1100 cm^{-1} are attributed to the stretching vibration of the carbonyl group (C=O) of carboxylic acid groups and C-OH in graphene oxide, respectively. The metal-oxgen bonds vibrations are represented by the peak observed at about 550-650 cm^{-1}. These peaks confirm the presence of both spinel structure and graphene oxide in the nanocomposite (Figs. 4, 5, 6) [17, 18].

The morphology and structure of the spinel nanoparticles embedded on graphene oxide sheets were examined using scanning electron microscopy (SEM). The SEM micrographs revealed the successful incorporation of spinel nanoparticles onto the GO sheets, forming well-dispersed nanocomposite structures. For the Fe_3O_4/GO nanocomposite, quasi-spherical Fe_3O_4 nanoparticles with an average diameter of 15-20 nm were uniformly distributed across the wrinkled GO matrix. The $CoFe_2O_4$/GO nanocomposite displayed cubic-shaped $CoFe_2O_4$ nanoparticles with sizes of 15-30 nm densely covering and interconnecting with the GO sheets. In the $NiFe_2O_4$/GO nanocomposite, spherical $NiFe_2O_4$ nanoparticles ranging from 20-40 nm in size were evenly anchored onto the GO surface, with some degree of aggregation observed (Figs. 7a, 7b, 7c). The SEM analysis provided visual evidence of the effective embedding of the spinel nanoparticles onto the GO sheets during synthesis [17, 18]. The nanocomposite structures exhibited good dispersion and anchoring of the nanoparticles, which can potentially enhance their adsorption properties and performance in heavy metal removal applications.

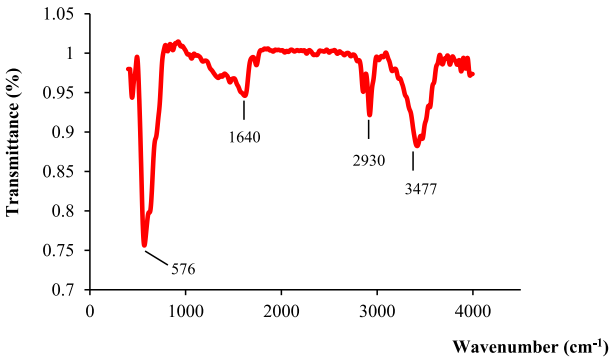

Figure 4. FT-IR spectra of Fe_3O_4/GO.

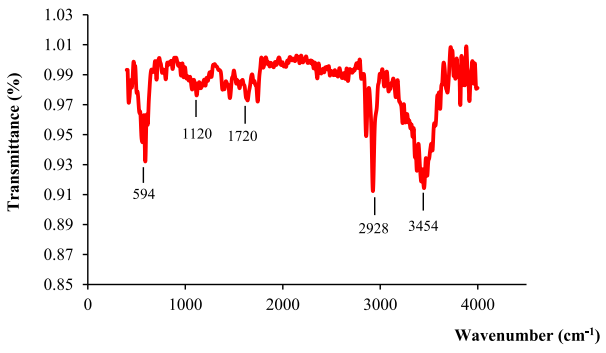

Figure 5. FT-IR spectra of $CoFe_2O_4$/GO.

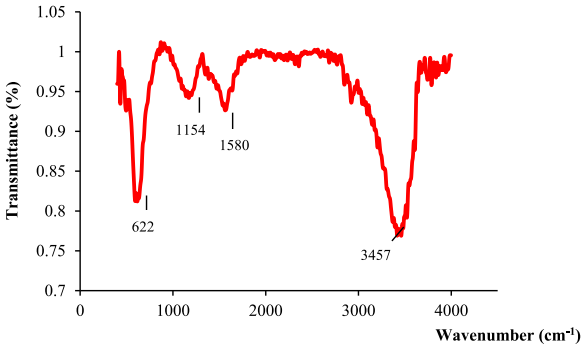

Figure 6. FT-IR spectra of $NiFe_2O_4$/GO.

3.1 Pb^{2+} adsorption

The pH of a solution significantly impacts the removal efficiency of Pb^{2+} ions. Under acidic conditions, an abundance of H^+ ions leads to an increase in the surface charge and possibility complexation [19–21]. At low pH, lead compounds become more soluble due to excess protons (H^+), which compete with lead ions for binding sites, thereby reducing removal efficiency. On the contrary, high pH (alkaline conditions) decreases the solubility of lead compounds, leading to the formation of insoluble precipitates like $Pb(OH)_2$. However, it is crucial to note that extremely high pH values can increase solubility due to the formation of complex compounds. Therefore, determining the optimal pH range is essential for achieving the highest removal efficiency. Moderate alkaline conditions are often preferred, while extreme pH values tend to reduce efficiency. The adsorption efficiency of Pb^{2+} ions was investigated using Fe_3O_4/GO, $CoFe_2O_4$/GO, and $NiFe_2O_4$/GO composites at various pH values. The results revealed distinct levels of Pb^{2+} adsorption efficiency across the examined pH range. In the case of the Fe_3O_4/GO composite, the percentage of Pb^{2+} adsorption was 71.8% at pH 3, 73.2% at pH 4, 77.7% at pH 5, 75.5% at pH 6, and 74.6% at pH 7. The $CoFe_2O_4$/GO composite displayed higher Pb^{2+} adsorption percentages, yielding 86.8% at pH 3, 87.6% at pH 4, 88.4% at pH 5, 89.2% at pH 6, and 88.15% at pH 7. Notably, the $NiFe_2O_4$/GO composite exhibited even greater Pb^{2+} adsorption percentages, with values of 88.4% at pH 3, 90.1% at pH 4, 91.1% at pH 5, 92.7% at pH 6, and 91.8% at pH 7. These findings highlight the influence of both pH and the specific composite material on Pb^{2+} adsorption efficiency (Fig. 8). The $CoFe_2O_4$/GO and $NiFe_2O_4$/GO nanocomposites demonstrated superior Pb^{2+} adsorption performance compared to the Fe_3O_4/GO composite across the investigated pH range. Consequently, these nanoomposites exhibit substantial potential as effective adsorbents for Pb^{2+} removal, with pH conditions playing a crucial role in their overall performance.

The effect of Fe_3O_4/GO, $CoFe_2O_4$/GO, and $NiFe_2O_4$/GO nanocomposite dosage on Pb^{2+} adsorption efficiency was investigated. The results revealed a positive correlation between composite weight and Pb^{2+} adsorption efficiency for all three composites. For the Fe_3O_4/GO composite, in-

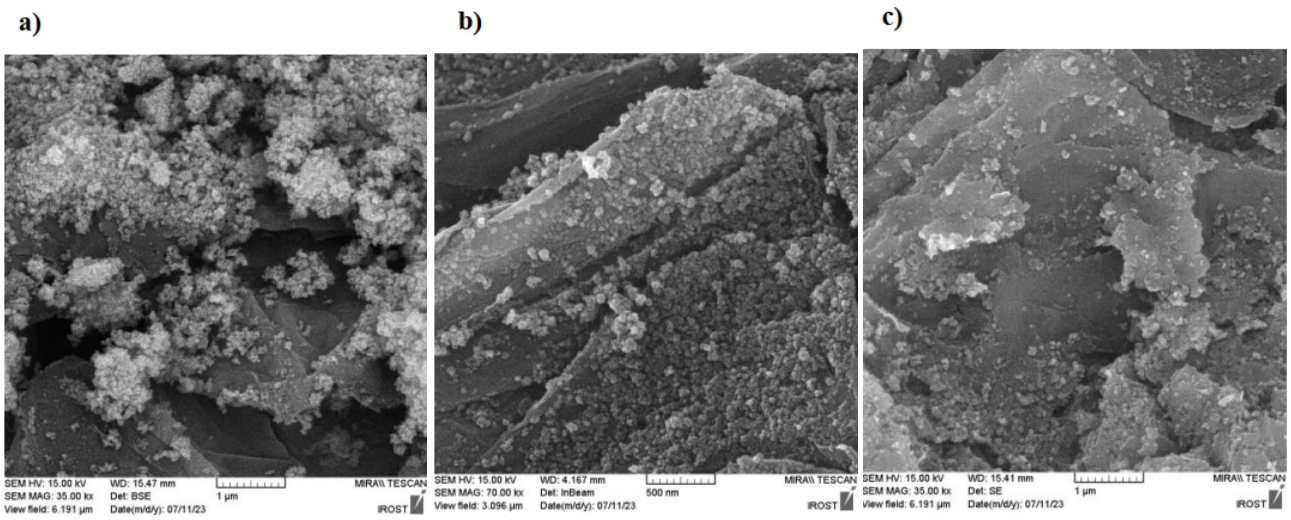

Figure 7. SEM images of a) Fe_3O_4/GO, b) $CoFe_2O_4$/GO, and c) $NiFe_2O_4$/GO.

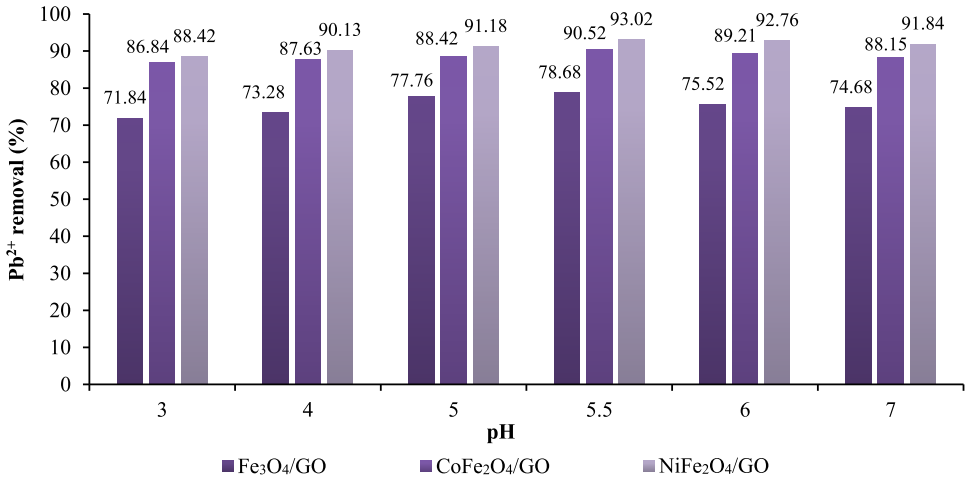

Figure 8. Effect of pH on Pb^{2+} removal.

creasing the composite weight from 0.01 g to 0.05 g led to a gradual increase in Pb^{2+} adsorption efficiency, with percentages ranging from 70.5% to 80.2%. Specifically, the adsorption percentages were 70.5% at 0.01 g, 74.3% at 0.02 g, 79.2% at 0.03 g, 79.7% at 0.04 g, and 80.2% at 0.05 g. The $CoFe_2O_4$/GO composite exhibited a similar trend, with Pb^{2+} adsorption percentages ranging from 79.9% to 83.4% as the composite weight increased from 0.01 g to 0.05 g. The adsorption percentages were 79.9% at 0.01 g, 82.0% at 0.02 g, 82.1% at 0.03 g, 82.7% at 0.04 g, and 83.4% at 0.05 g. Likewise, the $NiFe_2O_4$/GO composite showed increasing Pb^{2+} adsorption efficiency with higher composite weights. The percentages of Pb^{2+} adsorption ranged from 84.5% to 86.3%, corresponding to composite weights of 0.01 g to 0.05 g, respectively. The specific adsorption percentages were 84.5% at 0.01 g, 85.7% at 0.02 g, 86.0% at 0.03 g, 86.2% at 0.04 g, and 86.3% at 0.05 g (Fig. 9). These findings demonstrate that higher composite weights generally enhance Pb^{2+} adsorption efficiency across all three composites. Among the composites, the $NiFe_2O_4$/GO consistently exhibited the highest adsorption percentages, followed by the $CoFe_2O_4$/GO and Fe_3O_4/GO composites. In conclusion, increasing the weight of the Fe_3O_4/GO, $CoFe_2O_4$/GO, and $NiFe_2O_4$/GO composites positively influenced Pb^{2+} adsorption efficiency. Higher composite weights resulted in higher adsorption percentages, with the $NiFe_2O_4$/GO composite exhibiting the highest adsorption efficiency among the three composites investigated.

The study investigated the influence of contact time on removing Pb^{2+} ions using Fe_3O_4/GO, $CoFe_2O_4$/GO, and $NiFe_2O_4$/GO nanocomposites. The results revealed a positive correlation between contact time and the percentage of Pb^{2+} removal for each composite. For the Fe_3O_4/GO composite, the percentages of Pb^{2+} removal increased with longer contact times, ranging from 80.7% at 15 minutes to 88.8% at 75 minutes. Specifically, the removal percentages were 80.7% at 15 minutes, 83.8% at 30 minutes, 88.1% at 45 minutes, 88.4% at 60 minutes, and 88.8% at 75 min-

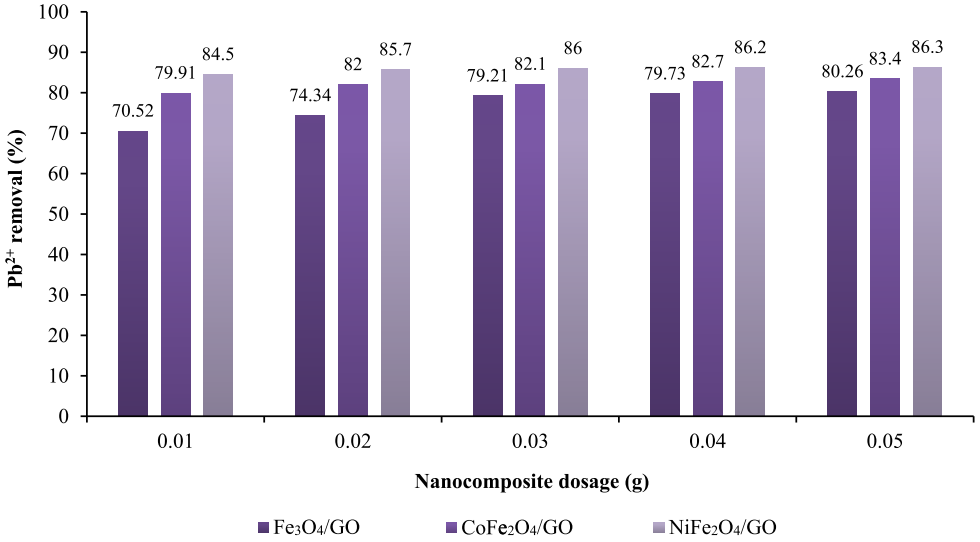

Figure 9. Effect of nanocomposites dosage on Pb^{2+} removal.

utes. The $CoFe_2O_4$/GO composite also displayed increasing percentages of Pb^{2+} removal with extended contact times, ranging from 82.9% at 15 minutes to 90.3% at 75 minutes. The removal percentages were 82.9% at 15 minutes, 86.2% at 30 minutes, 89.4% at 45 minutes, 89.7% at 60 minutes, and 90.3% at 75 minutes. Similarly, the $NiFe_2O_4$/GO composite demonstrated a consistent trend of improved Pb^{2+} removal efficiency with longer contact times, ranging from 93.5% at 15 minutes to 96.1% at 75 minutes. The removal percentages were 93.5% at 15 minutes, 95.1% at 30 minutes, 95.5% at 45 minutes, 95.9% at 60 minutes, and 96.1% at 75 minutes (Fig. 10). These findings suggest that prolonging the contact time between the composites and the Pb^{2+} solution enhances the efficiency of Pb^{2+} removal across all three composites. Among the composites, the $NiFe_2O_4$/GO consistently exhibited the highest percentages of Pb^{2+} removal across all contact times, followed by the $CoFe_2O_4$/GO composite. The Fe_3O_4/GO composite displayed slightly lower but still notable levels of Pb^{2+} removal. In conclusion, the study highlights the importance of increasing contact time to enhance the efficiency of Pb^{2+} removal using the Fe_3O_4/GO, $CoFe_2O_4$/GO, and $NiFe_2O_4$/GO composites. The $NiFe_2O_4$/GO composite demonstrated the highest percentages of Pb^{2+} removal, followed by the $CoFe_2O_4$/GO and Fe_3O_4/GO nanocomposites.

The continuing aimed to investigate how the concentration of lead in the solution affects the removal efficiency of Pb^{2+} using Fe_3O_4/GO, $CoFe_2O_4$/GO, and $NiFe_2O_4$/GO composites. The results revealed notable variations in Pb^{2+} removal efficiency across different lead concentrations for each composite. For the Fe_3O_4/GO composite, the percentages of P^{2+} removal increased with higher lead concentrations up to 20 ppm, after which the removal efficiency declined. The specific removal percentages were 81.4% at 5 ppm, 85.6% at 10 ppm, 89.2% at 20 ppm, 88.8% at 30 ppm, and 84.8% at 40 ppm. In the case of the $CoFe_2O_4$/GO composite, the percentages of Pb^{2+} removal followed a similar trend, with higher removal efficiency observed up to 10

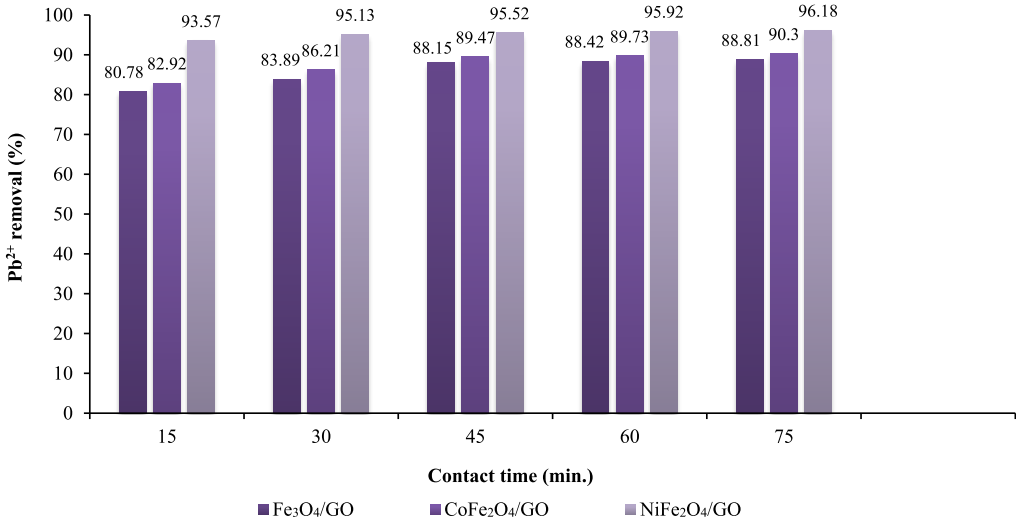

Figure 10. Effect of contact time on Pb^{2+} removal.

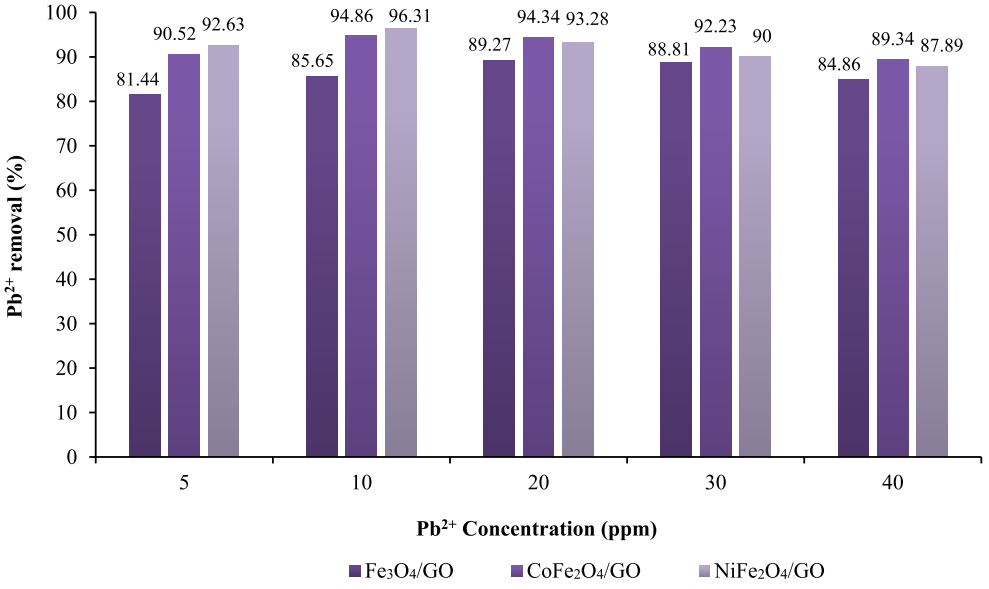

Figure 11. Effect of Pb^{2+} concentration on Pb^{2+} removal.

ppm, and then a gradual decline. The removal percentages were 90.5% at 5 ppm, 94.8% at 10 ppm, 94.3% at 20 ppm, 92.2% at 30 ppm, and 89.3% at 40 ppm. Similarly, for the $NiFe_2O_4$/GO composite, the percentages of Pb^{2+} removal increased with higher lead concentrations up to 10 ppm, after which the removal efficiency decreased. The specific removal percentages were 92.6% at 5 ppm, 96.3% at 10 ppm, 93.2% at 20 ppm, 90.0% at 30 ppm, and 87.8% at 40 ppm (Fig. 11). These findings indicate that the efficiency of Pb^{2+} removal is significantly influenced by the concentration of lead in the solution. In general, higher lead concentrations resulted in increased removal percentages, reaching a peak at a certain point (10-20 ppm), beyond which the removal efficiency started to decline. This trend was observed across all three composites. Among the composites, the $CoFe_2O_4$/GO consistently exhibited the highest Pb^{2+} removal percentages across most lead concentrations. The $NiFe_2O_4$/GO composite also demonstrated significant removal efficiency, particularly at lower lead concentrations. On the other hand, the Fe_3O_4/GO composite displayed slightly lower removal percentages than the other two composites. Therefore, the removal efficiency of Pb^{2+} using the Fe_3O_4/GO, $CoFe_2O_4$/GO, and $NiFe_2O_4$/GO composites is strongly influenced by the lead concentration in the solution. The $CoFe_2O_4$/GO composite generally exhibited the highest removal percentages, followed by the $NiFe_2O_4$/GO composite. The optimal lead concentration for maximum removal efficiency varied among the composites but typically ranged between 10-20 ppm.

3.2 Kinetics study

To assess the adsorption efficiency, kinetic models such as the pseudo-first-order and pseudo-second-order equations are commonly employed. The pseudo-first-order kinetic equation is shown by equation 1:

$$\ln(q_e - q_t) = \ln(q_e) - k_1 t \quad (1)$$

In equation 1, q_e and q_t represent the adsorption capacity at equilibrium and at different times, respectively. The rate constant of the pseudo-first-order model for the adsorption process is denoted by k_1 (min^{-1}).

On the other hand, the pseudo-second-order model suggests that the rate-limiting step of adsorption is chemisorption, where adsorption can occur at sites where no interactions between the adsorbates occur. This model is represented by equation 2:

$$t/q_t = 1/(k_2 q_e^2) + t/q_e \quad (2)$$

In equation 2, k_2 ($g{\cdot}mg^{-1}{\cdot}min^{-1}$) is the rate constant for pseudo-second-order adsorption.

The pseudo-first-order model yielded R^2 values of 0.86, 0.62, and 0.77 for Fe_3O_4/GO, $CoFe_2O_4$/GO, and $NiFe_2O_4$/GO, respectively, in Pb^{2+} removal. In contrast, the R^2 values for the pseudo-second-order model using Fe_3O_4/GO, $CoFe_2O_4$/GO, and $NiFe_2O_4$/GO were 0.99, 0.99, and 1.00 (Figs. 12a, 12b, 12c). The results indicated that the second-order kinetic model provided a better fit for both nanocomposites. The higher R^2 values obtained for the second-order model suggested it more accurately described the adsorption kinetics. Consequently, it can be concluded that the pseudo-first-order model is not highly accurate for this system. On the other hand, the pseudo-second-order model showed optimal outcomes and demonstrated effectiveness for Pb^{2+} removal (Figs. 12d, 12e, 12f).

3.3 Adsorption isotherm study

Adsorption isotherms offer valuable insights into surface characteristics and adsorption mechanisms. For the purpose of describing the adsorption mechanism in this study, the Temkin, Freundlich, and Langmuir isotherms were utilized. The Temkin isotherm can be represented in a linear form, as shown in Figs. 13a, 13b, 13c, by the equation 3:

$$q_e = RT/b \ln K_T + RT/b \ln C_e \quad (3)$$

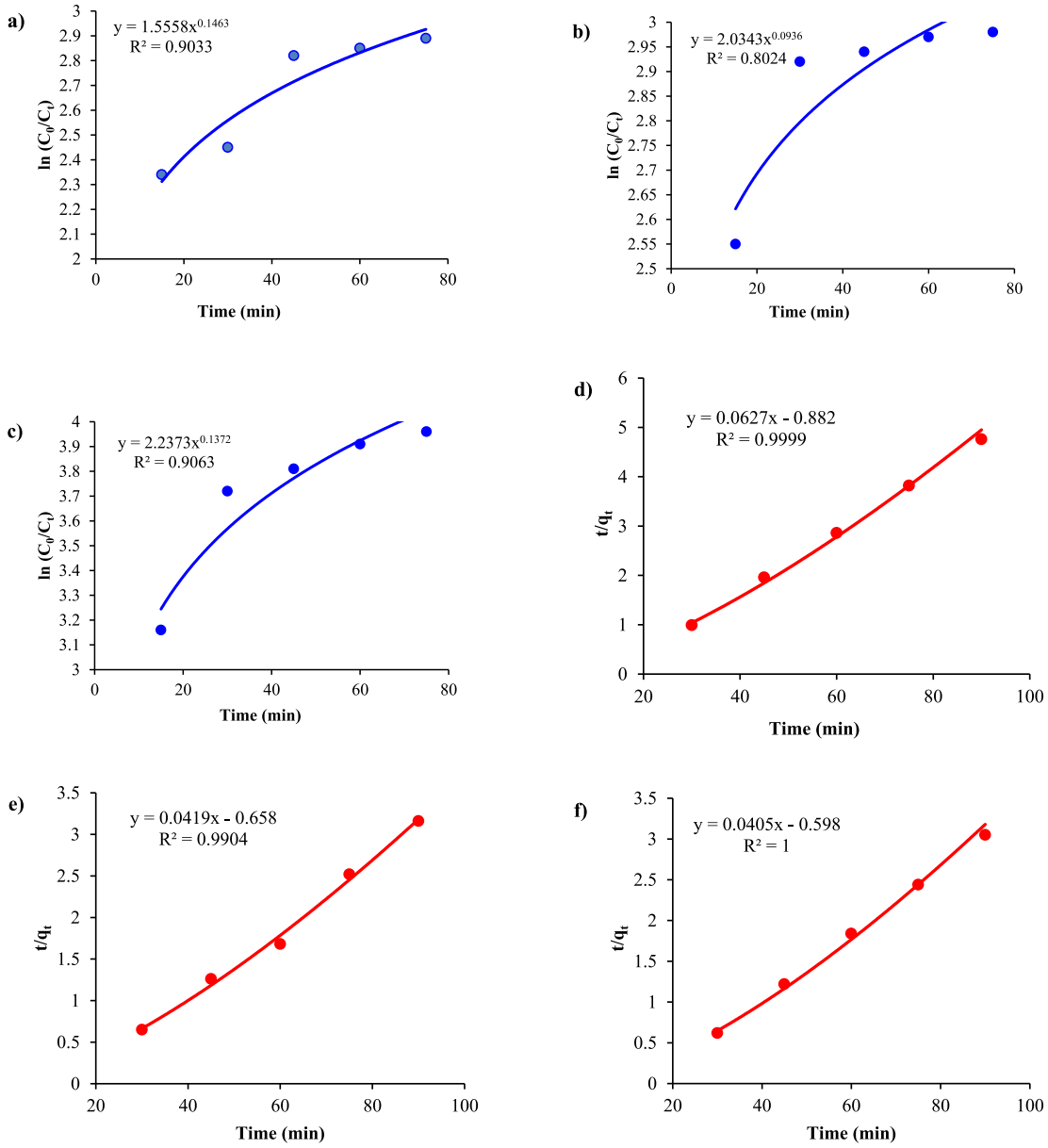

Figure 12. Kinetic studies of a,b,c) Pseudo-first-order and d,e,f) Pseudo-second order using Fe_3O_4/GO, $CoFe_2O_4$/GO, and $NiFe_2O_4$/GO on Pb^{2+} removal.

In the above equation, the values b, K, and R correspond to the Temkin constant (kJ·mol^{-1}), equilibrium binding constant (L·g^{-1}), and gas constant (8.314 J·mol^{-1}·K^{-1}), respectively. The Temkin isotherm model assumes a linear decrease in the adsorption heat of all molecules as the coverage of the adsorbent surface increases. This isotherm elucidates the interactions between the adsorbent and adsorbate.

The Freundlich isotherm can be expressed in linear form, as depicted in Figs. 14a, 14b, 14c, by the equation 4:

$$\log q_e = \log K_f + 1/n \log C_e \quad (4)$$

In the above equation, $1/n$ and K_f represent the Freundlich constants for adsorption intensity and adsorption capacity per unit concentration, respectively. This model is applicable to reversible and monolayer adsorption, wehich can be explained by multiple-layer adsorption on heterogeneous surfaces.

The Langmuir isotherm is illustrated as shown in Figs. 15a, 15b, 15c, and its equation 5 is:

$$1/q_e = 1/Q_{max} + 1/K_L Q_{max}(1/C_e) \quad (5)$$

Here, C_e (mg·L^{-1}) and q_e (mg·g^{-1}) denote the dye concentration in solution and the quantity of dye adsorbed per unit mass of nanocomposite at equilibrium, respectively. Q_{max} (mg·g^{-1}) represents the maximum adsorption capacity, while K_L (L·mg^{-1}) describes the Langmuir constant. Based on the correlation coefficient (R^2), the Langmuir adsorption isotherm demonstrates the best fit. According to this model, adsorption takes place within homogeneous sites

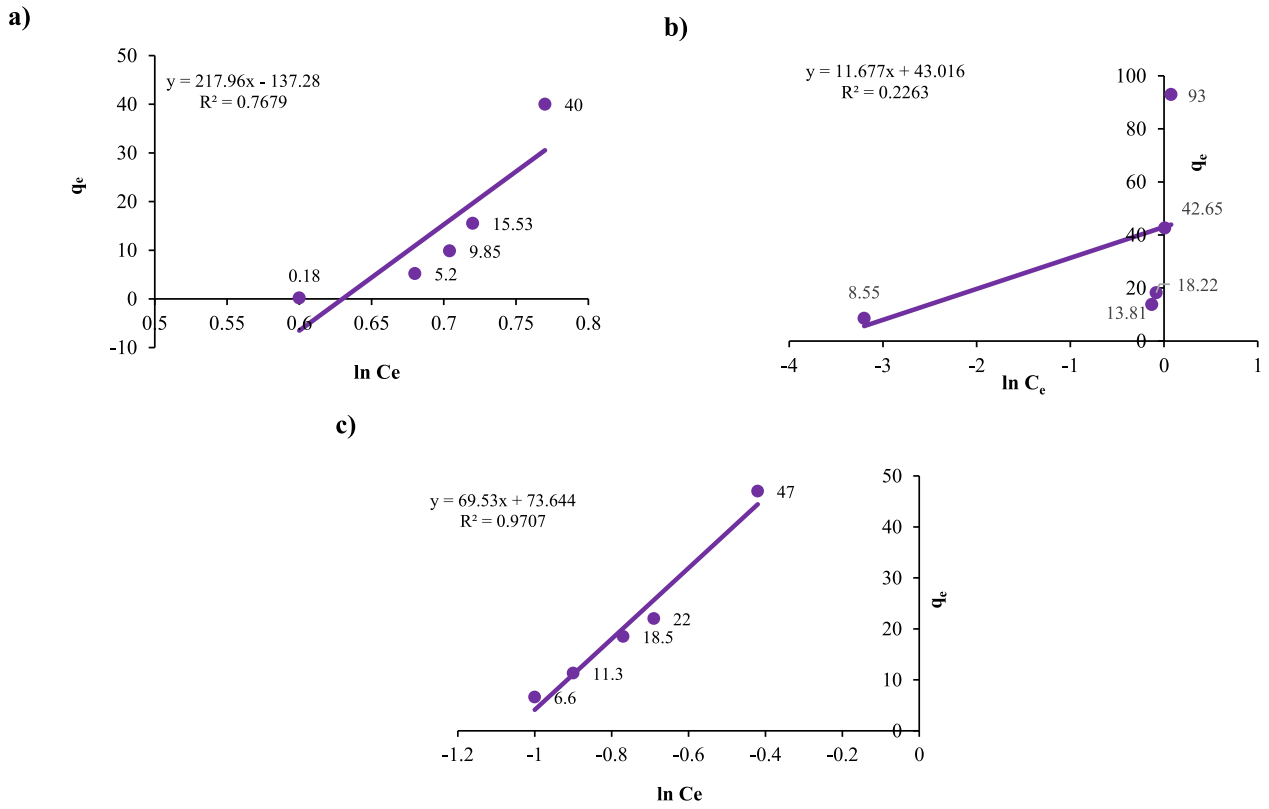

Figure 13. Temkin isotherms of Pb^{2+} removal using a) Fe_3O_4/GO, b) $CoFe_2O_4$/GO, and c) $NiFe_2O_4$/GO.

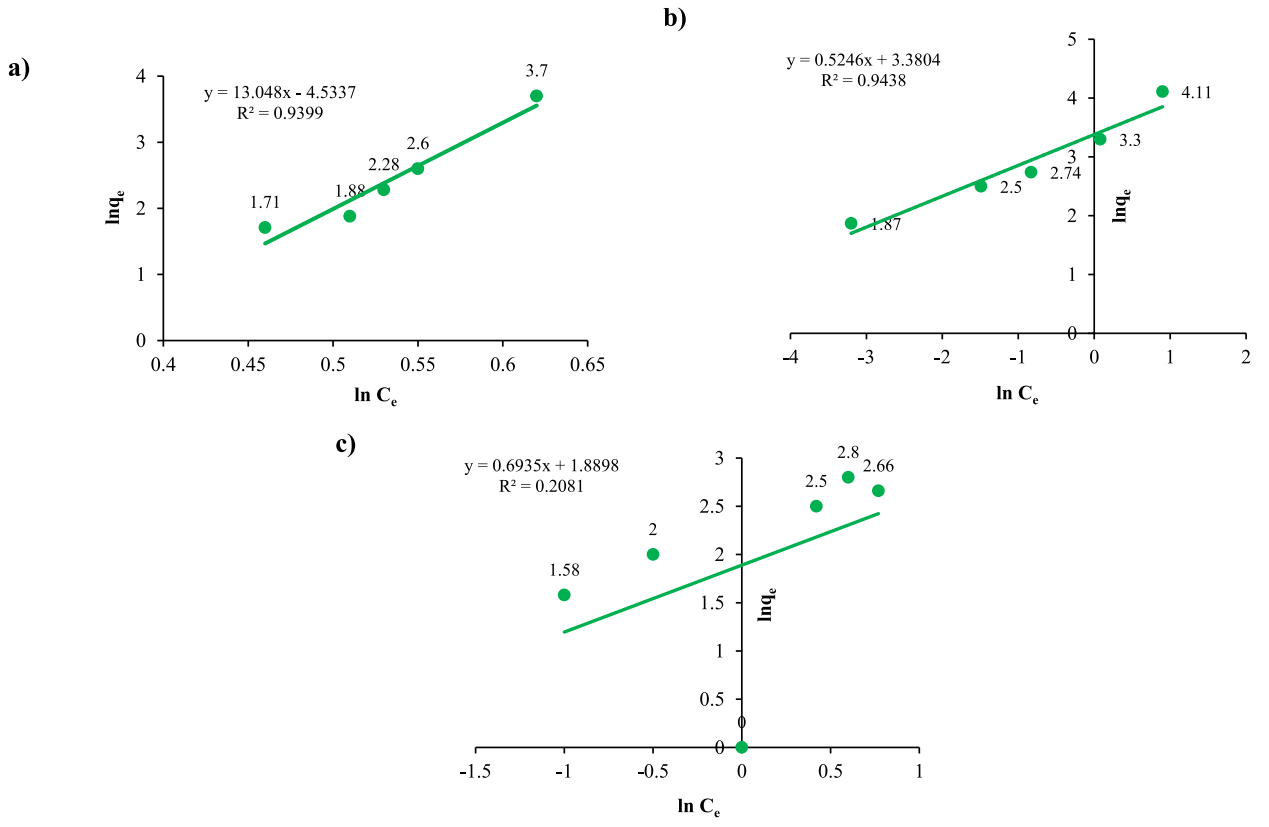

Figure 14. Freundlich isotherms of Pb^{2+} removal using a) Fe_3O_4/GO, b) $CoFe_2O_4$/GO, and c) $NiFe_2O_4$/GO.

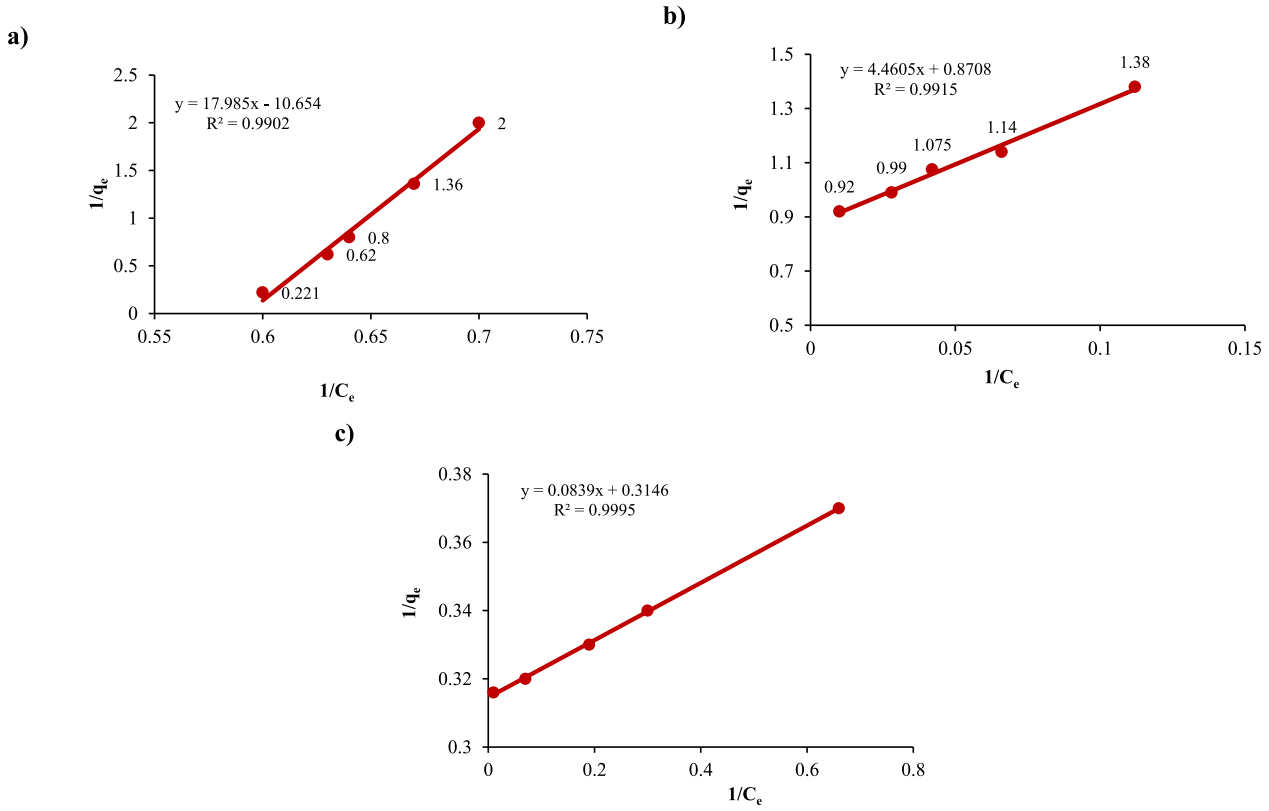

Figure 15. Langmuir isotherms of Pb^{2+} removal using a) Fe_3O_4/GO, b) $CoFe_2O_4$/GO, and c) $NiFe_2O_4$/GO.

on the adsorbent without transference through the surface.

3.4 Pb^{2+} removal mechanism

The removal mechanism of Pb^{2+} using spinel-embedded graphene oxide nanocomposites involves a combination of physical and chemical processes. These nanocomposites, consisting spinel nanoparticles like Fe_3O_4, $CoFe_2O_4$, or $NiFe_2O_4$ embedded with graphene oxide sheets, serve as highly efficient adsorbents for Pb^{2+} ions. The large surface area and abundance of functional groups (e.g., hydroxyl and carboxyl groups) on the GO sheets enable interactions with Pb^{2+} ions through electrostatic attractions and coordination bonding. This allows for the adsorption of Pb^{2+} ions onto the nanocomposite surface. Also, the presence of spinel nanoparticles within the nanocomposite enhances its removal capacity. The spinel nanoparticles embedded in the GO matrix contribute to the overall adsorption capacity. These nanoparticles provide additional active sites for Pb^{2+} ion adsorption due to their high surface area and unique crystal structure. Therefore, the mechanism of Pb^{2+} removal using spinel-embedded graphene oxide nanocomposites involves surface adsorption. The combination of GO's adsorption capability and spinel nanoparticles' properties results in a practical approach for removing Pb^{2+} ions from aqueous solutions.

3.5 Regeneration and reusability

The reusability of spinel nanostructure embedded graphene oxide is a significant advantage of this nanocomposite material. By incorporating spinel nanoparticles like Fe_3O_4, $CoFe_2O_4$, or $NiFe_2O_4$ into the GO matrix, not only does it exhibit efficient adsorption capabilities, but it also allows for easy recovery and recycling. The magnetic properties of the spinel nanoparticles enable the nanocomposite to be easily separated from the solution using an external magnetic field. This magnetic separation process facilitates the selective recovery of the spinel-embedded graphene oxide while leaving the treated solution free of the adsorbent. The recovered nanocomposite was washed or regenerated for subsequent reuse. The spinel-embedded graphene oxide nanocomposite has demonstrated exceptional recyclability in the adsorption-based removal of Pb^{2+}. Even after undergoing three consecutive usage cycles, the nanocomposite maintains an impressive removal efficiency of over 65%. This highlights the material's robust performance and ability to maintain its adsorption capacity over multiple reuse cycles. The recyclability of the nanocomposite makes it a sustainable and cost-effective solution for Pb^{2+} removal, offering long-term utility without compromising its effectiveness.

The synthesized Fe_3O_4/GO, $CoFe_2O_4$/GO, and $NiFe_2O_4$/GO nanocomposites offer cost-effective advantages. The starting materials and synthesis methods like hydrothermal are relatively inexpensive and scalable. Their magnetic properties enable easy separation and adsorbent recovery using an external magnetic field, eliminating costly filtration/centrifugation steps. Their excellent recyclability, maintaining over 65% removal efficiency after three cycles, minimizes frequent adsorbent replacement and waste. Their high adsorption capacities

translate to lower adsorbent requirements for a given water volume. While initial synthesis costs may be slightly higher than conventional adsorbents, their superior performance, recyclability, and reduced operational costs make them cost-effective solutions, especially for treating large volumes of lead-contaminated water.

4. Conclusion

This study explores the use of spinel nanostructures-embedded graphene oxide nanocomposites (Fe_3O_4/GO, $CoFe_2O_4$/GO, and $NiFe_2O_4$/GO) as adsorbents for removing toxic Pb^{2+} ions from water. The main findings indicate that the $NiFe_2O_4$/GO nanocomposite exhibited the highest Pb^{2+} adsorption capacity, with 96.1% removal achieved within 75 minutes at an initial Pb^{2+} concentration of 10 ppm. The $CoFe_2O_4$/GO nanocomposite achieved 90.3% removal under similar conditions, while Fe_3O_4/GO showed 88.8%. The adsorption process followed a pseudo-second-order model, suggesting chemisorption as the rate-limiting step. The study highlights the advantages of combining graphene oxide's surface area and functional groups with the magnetic properties of spinel nanoparticles to create efficient adsorbents for heavy metal removal. The nanocomposite approach demonstrated superior performance compared to studies using individual components. The nanocomposites also exhibited good regeneration and reusability, maintaining over 65% removal efficiency after three cycles. Further research should focus on optimizing nanocomposite synthesis, understanding adsorption mechanisms at the molecular level, exploring selectivity towards other pollutants, conducting pilot-scale studies, and developing cost-effective synthesis methods. It is essential to consider the study's limitations, such as the need for evaluation under real-world conditions and assessing long-term stability and potential leaching. Overall, this study contributes to the design of effective adsorbents for heavy metal removal, addressing environmental and public health challenges and promoting sustainable water treatment solutions.

Authors Contributions
All authors have contributed equally to prepare the paper.

Availability of Data and Materials
The data that support the findings of this study are available from the corresponding author upon reasonable request.

Conflict of Interests
The authors declare that they have no known competing financial interests or personal relationships that could have appeared to influence the work reported in this paper.

References

[1] C. K. Swain. "Environmental pollution indices: A review on concentration of heavy metals in air, water, and soil near industrialization and urbanization.". *Discover Environ*, **2**:5–9, 2024. DOI: https://doi.org/10.1007/s44274-024-00030-8.

[2] S. Das, K. W. Sultana, A. R. Ndhlala, M. Mondal, and I. Chandra. "Heavy Metal Pollution in the Environment and Its Impact on Health: Exploring Green Technology for Remediation.". *Environ. Health Insights*, **17**:1–10, 2023. DOI: https://doi.org/10.1177/11786302231201259.

[3] A. L. Wani, A. Ara, and J. A. Usmani. "Lead toxicity: A review.". *Interdiscip. Toxicol*, **8**:55–64, 2015. DOI: https://doi.org/10.1515/intox-2015-0009.

[4] Z. Raji, A. Karim, A. Karam, and S. Khalloufi. "Adsorption of heavy metals: mechanisms, kinetics, and applications of various adsorbents in wastewater remediation-a review.". *Waste*, **1**:775–805, 2023. DOI: https://doi.org/10.3390/waste1030046.

[5] N.S. Hosseini, S. Sobhanardakani, M. Cheraghi, B. Lorestani, and H. Merrikhpour. "Heavy metal concentrations in roadside plants (Achillea wilhelmsii and Cardaria draba) and soils along some highways in Hamedan, west of Iran.". *Environ. Sci. Pollut. Res*, **27**:13301–13314, 2020. DOI: https://doi.org/10.1007/s11356-020-07874-6.

[6] S. Sobhanardakani, M. Ahmadi, and R. Zandipak. "Efficient removal of Cu(II) and Pb(II) heavy metal ions from water samples using 2, 4-dinitrophenylhydrazine loaded sodium dodecyl sulfate-coated magnetite nanoparticles.". *J. Water Supply: Res. Technol.-AQUA*, **65**:361–372, 2016. DOI: https://doi.org/10.2166/aqua.2016.100.

[7] A.H. Omidi, M. Cheraghi, B. Lorestani, S. Sobhanardakani, and A. Jafari. "Biochar obtained from cinnamon and cannabis as effective adsorbents for removal of lead ions from water.". *Environ. Sci. Pollut. Res*, **26**:27905–27914, 2019. DOI: https://doi.org/10.1007/s11356-019-05997-z.

[8] M. Soylak, O. Ozalp, and F. Uzcan. "Magnetic nanomaterials for the removal, separation and preconcentration of organic and inorganic pollutants at trace levels and their practical applications: A review.". *Trends Environ. Anal. Chem*, **29**:e00109, 2021. DOI: https://doi.org/10.1016/j.teac.2020.e00109.

[9] M. Soylak, M. Alasaad, and Ö. Özalp. "Fabrication and characterization of $MgCo_2O_4$ for solid phase extraction of Pb(II) from environmental samples and its detection with high-resolution continuum source flame atomic absorption spectrometry (HR-CS-FAAS).". *Microchem. J*, **178**:107329, 2022. DOI: https://doi.org/10.1016/j.microc.2022.107329.

[10] F. Uzcan and M. Soylak. "$CuCo_2O_4$ as affective adsorbent for dispersive solid phase extraction of lead from food, cigarette and water samples before FAAS detection.". *Chem. Pap*, **75**:6367–6375, 2021. DOI: https://doi.org/10.1007/s11696-021-01797-3.

[11] T. K. Sen. "Agricultural solid wastes based adsorbent materials in the remediation of heavy metal ions from water and wastewater by adsorption: A review.". *Molecules*, **28**:5575–5579, 2023. DOI: https://doi.org/10.3390/molecules28145575.

[12] S. D. Gisi, G. Lofrano, M. Grassi, and M. Notarnicola. "Characteristics and adsorption capacities of low-cost sorbents for wastewater treatment: A review.". *Sustain. Mater. Technol*, **9**:10–40, 2016. DOI: https://doi.org/10.1016/j.susmat.2016.06.002.

[13] Z. Iqbal, M. S. Tanweer, and M. Masood Alam. "Reduced graphene oxide-modified spinel cobalt ferrite nanocomposite: synthesis, characterization, and its superior adsorption performance for dyes and heavy metals.". *ACS Omega*, **8**:6376–6390, 2023. DOI: https://doi.org/10.1021/acsomega.2c06636.

[14] P. L. Narayana, L. P. Lingamdinne, R. R. Karri, S. Devanesan, M. S. AlSalhi, N. S. Reddy, Y. Y. Chang, and J. R. Koduru. "Predictive capability evaluation and optimization of Pb(II) removal by reduced graphene oxide-based inverse spinel nickel ferrite nanocomposites.". *Environ. Res*, **204**:112029, 2022. DOI: https://doi.org/10.1016/j.envres.2021.112029.

[15] R. Kumar, S. Bhattacharya, and P. Sharma. "Novel insights into adsorption of heavy metal ions using magnetic graphene composites.". *J. Environ. Chem. Eng*, **9**:106212, 2021. DOI: https://doi.org/10.1016/j.jece.2021.106212.

[16] L. P. Lingamdinne, J. R. Koduru, Y. L. Choi, Y. Y. Chang, and J. K. Jae-Kyu Yang. "Studies on removal of Pb(II) and Cr(III) using graphene oxide based inverse spinel nickel ferrite nano-composite as sorbent.". *Hydrometallurgy*, **165**:64–72, 2016. DOI: https://doi.org/10.1016/j.hydromet.2015.11.005.

[17] M. Parastar Gharehlar, S. Sheshmani, F. R. Nikmaram, and Z. Doroudi. "Assessing the efficacy of iron (II, III) oxide nanocomposites for the photodegradation of organic dye pollutants and textile wastewater under UV-visible irradiation.". *Chem. Pap*, **3**:2015–2032, 2023. DOI: https://doi.org/10.1007/s11696-023-03223-2.

[18] M. Parastar Gharehlar, S. Sheshmani, F. R. Nikmaram, and Z. Doroudi. "Synergistic potential in spinel ferrite MFe_2O_4 (M = Co, Ni) nanoparticles-mediated graphene oxide: Structural aspects, photocatalytic, and kinetic studies.". *Sci. Rep*, **14**:4625–4629, 2024. DOI: https://doi.org/10.1038/s41598-024-55452-4.

[19] S. Hosseinzadeh, Eslami M. Moghadam, S. Sheshmani, and A.S. Shahvelayati. "Some new anticancer platinum complexes of dithiocarbamate derivatives against human colorectal and pancreatic cell lines.". *J. Biomol. Struct. Dyn*, **38**:2215–2228, 2020. DOI: https://doi.org/10.1080/07391102.2019.1627909.

[20] J. Soleimannejad, H. Aghabozorg, Y. Mohammadzadeh, M. Nasibipour, S. Sheshmani, A. Shokrollahi, E. Karami, and M. Shamsipure. "Different complexation behavior of Fe(III), Co(II) and Ni(II) with pyridine-2,6-dicarboxylic Acid and $4,4'$-bipyridine adduct: Syntheses, crystal structures and solution studies.". *J. Iran. Chem. Soc*, **8**:247–264, 2011. DOI: https://doi.org/10.1007/BF03246222.

[21] H. Aghabozorg, J. Soleimannejad, M. Sharif, S. Sheshmani, and A. Moghimi. "Crystal structure of a proton-transfer compound between 2,6-pyridinedicarboxylic acid and N,N'-diethyl-2-amino-6-methyl-4-pyrimidinol". *Anal. Sci. X-ray Struct. Anal*, **21**:x73–x74, 2005. DOI: https://doi.org/10.2116/analscix.21.x73.